ACS APPLIED MATERIALS & INTERFACES
Research Article
www.acsami.org

Electron-Beam-Induced Deposition as a Technique for Analysis of Precursor Molecule Diffusion Barriers and Prefactors

Jared Cullen, Charlene J. Lobo, Michael J. Ford, and Milos Toth*

School of Mathematical and Physical Sciences, University of Technology Sydney, Ultimo, New South Wales 2007, Australia

ABSTRACT: Electron-beam-induced deposition (EBID) is a direct-write chemical vapor deposition technique in which an electron beam is used for precursor dissociation. Here we show that Arrhenius analysis of the deposition rates of nanostructures grown by EBID can be used to deduce the diffusion energies and corresponding preexponential factors of EBID precursor molecules. We explain the limitations of this approach, define growth conditions needed to minimize errors, and explain why the errors increase systematically as EBID parameters diverge from ideal growth conditions. Under suitable deposition conditions, EBID can be used as a localized technique for analysis of adsorption barriers and prefactors.

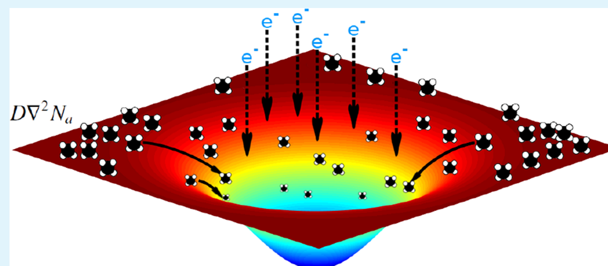

KEYWORDS: *electron-beam-induced deposition, adsorbate diffusion, reaction kinetics, surface chemistry*

INTRODUCTION

Electron-beam-induced deposition (EBID) is a direct-write chemical vapor deposition technique in which surface-adsorbed precursor molecules are dissociated by an electron beam.[1−5] It has been used to fabricate nanostructures such as optical nanoantennas,[6,7] nanoscale tunneling electrodes,[8] magnetic nanowires,[9] and electrical contacts to individual nanoribbons[10] and nanotubes.[11] In addition to nanofabrication, EBID [and the related technique of electron-beam-induced etching (EBIE)[2,12]] can also be used as a technique for analysis of the adsorbates (i.e., reagents) used in the deposition and etching reactions.[13−22] Molecular properties that can be measured are those that affect the rates of adsorption (e.g., sticking coefficients), desorption (energies and attempt frequencies), diffusion (barriers and prefactors), and dissociation (cross sections). The measurement procedure typically involves the fabrication of a number of nanostructures (deposits or etch pits) as a function of a control parameter such as temperature. The property of interest is then deduced using rate equations that relate the nanostructure growth rate to the control parameter. The ability of EBID and EBIE to measure the adsorbate properties is useful for two reasons. First, the techniques are complementary to and have some advantages over conventional adsorbate characterization techniques. Second, the adsorbate properties can be used as input parameters for models used to simulate EBID and EBIE. This is important because the models play a key role in improving the understanding and capabilities of these nanofabrication techniques but are often limited by inadequate knowledge of input parameters such as adsorption and diffusion energies.[1,2]

The use of EBID and EBIE as robust, reliable adsorbate characterization techniques requires careful quantitative analysis of the underlying mechanisms in order to identify, explain, and eliminate potential artifacts. For example, we recently used an accurate hybrid continuum−Monte Carlo simulation of EBID to show that the precursor molecule adsorption energy (E_a) and desorption attempt frequency (k_0) can be deduced by Arrhenius analysis of the deposition rates only if EBID is performed under appropriate conditions.[13] Here we use the same model to develop a procedure for determination of the diffusion barrier (E_D) and preexponential factor (D_0) by exploiting the fact that the precursor molecules consumed in EBID are replenished through two pathways: adsorption from the gas phase and diffusion along the surface. We show that diffusion gives rise to a growth rate component that can be isolated and that Arrhenius analysis of this growth rate component can be used to deduce E_D and D_0. The technique is compelling relative to conventional diffusion analysis techniques[23,24] because it yields both E_D and D_0 and can be combined with a related EBID Arrhenius technique[13] to obtain the corrugation factor (defined as the ratio of the diffusion energy and the adsorption energy) from a single set of self-consistent data with nanoscale spatial resolution.

We note that Utke et al.[19] and Szkudlarek et al.[16] previously used the deposit geometry to estimate the diffusion coefficient of $Cu(hfac)_2$. Fowlkes et al.[17] estimated the diffusion coefficient of $W(CO)_6$ by analysis of the growth rates of pillars fabricated by EBID using a pulsed electron beam. Here, we probe E_D and D_0 by measuring the dependence of the diffusion rate on the substrate temperature.

Received: July 14, 2015
Accepted: September 4, 2015
Published: September 4, 2015

ACS Publications © 2015 American Chemical Society

DOI: 10.1021/acsami.5b06341
ACS Appl. Mater. Interfaces 2015, 7, 21408−21415

BACKGROUND THEORY

The standard continuum EBID model defines the rate of change of the adsorbed precursor molecule concentration (N_a) over time and space:[1−3,12]

$$\frac{\partial N_a}{\partial t} = sF(1-\Theta) - \frac{N_a}{\tau} - \sigma f N_a + D\nabla^2 N_a \tag{1}$$

Here, t is time, and we use cylindrical coordinates (appropriate for a stationary electron beam that is not scanned across the surface), where r is the radial distance from the beam axis. N_a is a function of r and evolves in time once the electron beam is switched on, forming a deposit that grows on the substrate surface. The individual terms are fluxes (in units of molecules/Å^2/s) that represent adsorption from the gas phase [$sF(1-\Theta)$], desorption (N_a/τ), electron-induced dissociation ($\sigma f N_a$), and adsorbate diffusion along the surface ($D\nabla^2 N_a$). The maximum precursor concentration of adsorbed molecules is generally limited to one monolayer by $sF(1-\Theta)$, where s is the sticking coefficient from the gas phase, F is the precursor flux, and Θ is the surface coverage. The residence time τ is a function of E_a and k_0:

$$\tau = \frac{1}{k_0}\exp\left(\frac{E_a}{k_B T}\right) \tag{2}$$

where k_B is Boltzmann's constant and T is the substrate temperature. The dissociation term accounts for adsorbate decomposition by electrons, where σ is the net effective cross section for all reaction pathways and $f(r)$ is the electron flux profile. The last term accounts for adsorbate diffusion, and the diffusion coefficient (D) has an exponential dependence on temperature:

$$D = D_0 \exp\left(\frac{-E_D}{k_B T}\right) \tag{3}$$

where E_D is the energy barrier for diffusion and the preexponential factor D_0 is the diffusion coefficient in the limit $E_D \to 0$.

The vertical deposition rate, R (in units of Å/s), is given by

$$R = V\sigma f N_a \tag{4}$$

where V is the volume of a single molecule of the EBID reaction product deposited on the surface.

Solutions of eq 1 yield $N_a(r,t)$, which can then be used to calculate $R(r,t)$ and the corresponding volumetric deposition rate (R_V), which is obtained by integrating R over r. Below, we will show that R_V has a distinct component (R_{VD}) caused by diffusion of surface-adsorbed precursor molecules and that Arrhenius analysis of R_{VD} can be used to extract both E_D and D_0.

SIMULATION METHODOLOGY

EBID simulations were performed using an iterative, hybrid continuum−Monte Carlo model detailed in ref 13. We use the model to analyze the diffusion of adsorbates during EBID and to develop and test a method for the determination of E_D and D_0. The hybrid model iteratively solves eq 1 to find $R(r,t)$, advances t by a small time interval Δt, evolves the growing substrate surface, and calculates the electron flux profile $f(r,t)$ corresponding to the growing deposit using a Monte Carlo simulator of electron−solid interactions. The hybrid model is both accurate and sufficiently fast to enable simulation of EBID over the length and temporal scales encountered in experiments.[13]

We use the hybrid model to simulate EBID of the precursor cyclopentadienyltrimethylplatinum using a 5 keV, 1 nA, stationary Gaussian electron beam with a diameter of 100 nm, a diffusion energy and a preexponential factor of 114 meV and 4.16×10^9 Å^2/s, respectively, and substrate temperatures in the range of 120−350 K. The diffusion energy and preexponential factor used here were respectively reported in the work by Shen et al.[25] and Winkler et al.[26] (the values were assumed to be the same on the growing deposit and the substrate). All other model input parameters and extensive tests used to validate the model are provided in the Supporting Information of ref 13. Langmuir adsorption is assumed at all temperatures; hence, precursor condensation that occurs at low temperatures is ignored by the model. This point is discussed further below.

RESULTS AND DISCUSSION

Roles of Desorption and Diffusion in EBID. Equations 2 and 3 show that the desorption time and diffusion coefficient have exponential dependencies on the temperature. We have previously demonstrated[13] that Arrhenius analysis of the EBID rates can be used to obtain the adsorption energy and desorption attempt frequency. Specifically, we showed that under appropriate conditions eq 4 can be approximated by

$$R \approx V\sigma f s F \tau \tag{5}$$

$$R \approx V\sigma f s F \tau_0 \exp\left(\frac{E_a}{k_B T}\right) \tag{6}$$

and a plot of ln(R) versus $1/T$ is linear and has a slope of $E_a/k_B T$ and a y intercept of $V\sigma f s F \tau_0$. Equation 5 is valid only in the so-called *reaction-rate-limited growth regime*,[1] where adsorbate depletion caused by the electron beam is negligible. In this regime, diffusion plays a negligible role in the replenishment of adsorbates consumed in EBID.[13] However, in the opposite extreme of high depletion (encountered at high electron-beam-current densities), diffusion can make a very significant contribution to EBID.[1,17,19] This is illustrated in Figure 1a, which shows cross-sectional slices through deposits simulated at a number of temperatures. At the lowest temperature shown in the figure, the deposit has a flat-top geometry because D is negligible, and precursor adsorbates under the Gaussian electron beam are highly depleted; i.e. within the flat region of the deposit, the vast majority of molecules adsorbing through sF are consumed in EBID through $\sigma f N_a$. At elevated temperatures, each deposit contains a characteristic "ring" generated by adsorbates supplied through surface diffusion (i.e., through the term $D\nabla^2 N_a$ in eq 1). The ring is also seen in the steady-state vertical deposition rates $R(r)$ shown in Figure 1b for a number of temperatures T_n. In the following, we demonstrate that Arrhenius analysis of the volumetric growth rate of this ring can be used to obtain E_D and D_0.

Adsorbate Transport through Diffusion. The diffusion flux in eq 1 yields the net transport of adsorbates across the surface. It consists of a diffusion coefficient, D, multiplied by the driving force of diffusion, $\nabla^2 N_a$. The latter relates the net flow of adsorbates across the surface to the adsorbate concentration gradient at each point on the surface. In cylindrical coordinates, the driving force of diffusion, represented from here on by c, is given by

DOI: 10.1021/acsami.5b06341
ACS Appl. Mater. Interfaces 2015, 7, 21408−21415

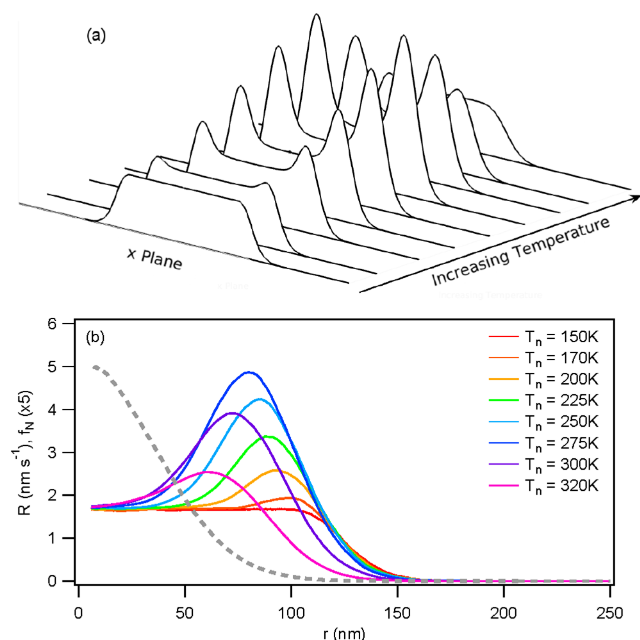

Figure 1. Effects of diffusion on the shapes of deposits grown by EBID. (a) A series of deposits simulated as a function of temperature. At low temperatures, the deposit geometry is unaffected by diffusion, but at elevated temperatures, each deposit contains a characteristic "ring" generated by adsorbates supplied through surface diffusion. (b) Steady-state vertical growth rates (R) calculated as a function of the distance (r) from the electron beam axis at a number of temperatures (T_n). All simulations were performed using a Gaussian electron beam under conditions of high adsorbate depletion near the beam axis. The normalized electron flux profile $f_N(r)$ is shown as a dashed curve in part b.

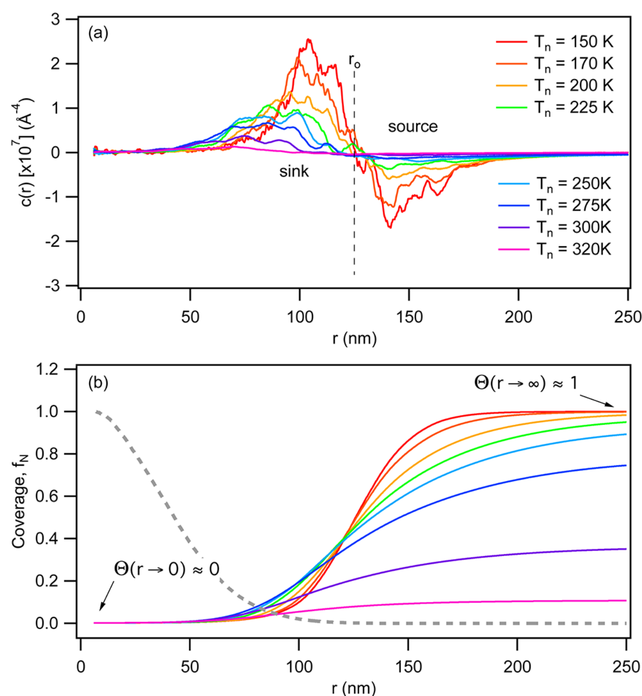

Figure 2. (a) Steady-state plots of the driving force of diffusion (c) versus distance (r) from the electron beam axis at a number of temperatures (T_n). Each $c(r)$ profile contains two distinct regions corresponding to the source and sink of adsorbates that diffuse along the surface and are consumed in EBID. The sink and source are separated by r_0, shown as a dashed line at 125 nm. (b) Corresponding adsorbate coverage profiles [$\Theta(r)$] and the normalized electron flux profile [($f_N(r)$; dashed gray curve].

$$c = \nabla^2 N_a = \frac{\partial^2 N_a}{\partial r^2} + \frac{1}{r}\frac{\partial N_a}{\partial r} \quad (7)$$

Because c and D appear as a product in eq 1, the dependence of c on r and T must be understood if we are to develop an Arrhenius analysis technique for the determination of E_D and D_0.

Figure 2a shows $c(r)$ profiles corresponding to the $R(r)$ profiles in Figure 1b at a number of temperatures T_n, simulated under conditions of significant depletion caused by the electron beam. The extent of depletion is illustrated in Figure 2b by plots of the surface coverage $\Theta(r)$ and the normalized electron flux profile $f_N(r)$. The plots of $c(r)$ show that it is comprised of two distinct regions separated by r_0: one positive (at $r < r_0$, where, in this particular case, $r_0 \sim 125$ nm) and the other negative (at $r > r_0$). To explain the dependence of c on r, we must consider how adsorbates are replenished during EBID. When electrons irradiate the substrate, an adsorbate concentration gradient (i.e., the coverage gradient seen in Figure 2b) forms as precursor molecules are consumed in the deposition reaction. The consumed adsorbates are replenished through adsorption from the gas phase and diffusion along the surface. The diffusing adsorbates originate in the negative part of $c(r)$, labeled "source" in Figure 2a, and are dissociated in the positive region, labeled "sink". The integral of $c(r)$ over the sink region ($0 \le r \le r_0$) is a fluence C (in units of Å^{-2}) corresponding to in-diffusing adsorbates that are dissociated by electrons and give rise to the formation of the rings seen in Figure 1. CD is therefore the corresponding growth rate, and the volumetric deposition rate of the rings (in units of Å^3/s) is therefore given by

$$R_{VD} = VCD \quad (8)$$

$$R_{VD} = VCD_0 \exp\left(\frac{-E_D}{k_B T}\right) \quad (9)$$

Equations 8 and 9 are analogous to eqs 5 and 6, and as we show below, a plot of $\ln(R_{VD}/C)$ versus $1/T_m$ can be used to obtain E_D and D_0, provided the quantity C is known at each of the temperatures T_m used to generate the Arrhenius plot. Arrhenius analysis must be performed on the quantity R_{VD}/C (rather than R_{VD}) because C is a function of T, as shown in Figure 3a. Corresponding plots of $R_{VD}(T)$ and $R_{VD}/C(T)$ are shown in parts b and c of Figure 3 and discussed below.

We note that the above arguments are valid only over a particular temperature window, shown in Figure 3, as is discussed in detail below.

Experimentally, C can be obtained at any given temperature T_n by measuring the deposition rate $R(r)$ and rearranging eq 4 to give $N_a(r)$:

$$N_a = R/V\sigma f \quad (10)$$

which can then be substituted into eq 7 to obtain $c(r)$. Integration of $c(r)$ over $0 \le r \le r_0$ gives C. Hence, at a given temperature T_n, a plot of $\ln(R_{VD}/C)$ versus $1/T_m$ can be obtained from the measured experimental growth rates ($R(r,T_m)$ and $R_V(T_m)$, where T_m represents a set of temperatures centered on T_n used to generate the Arrhenius plot (see, for example, the simulated Arrhenius plots shown in Figure 4).

DOI: 10.1021/acsami.5b06341
ACS Appl. Mater. Interfaces 2015, 7, 21408−21415

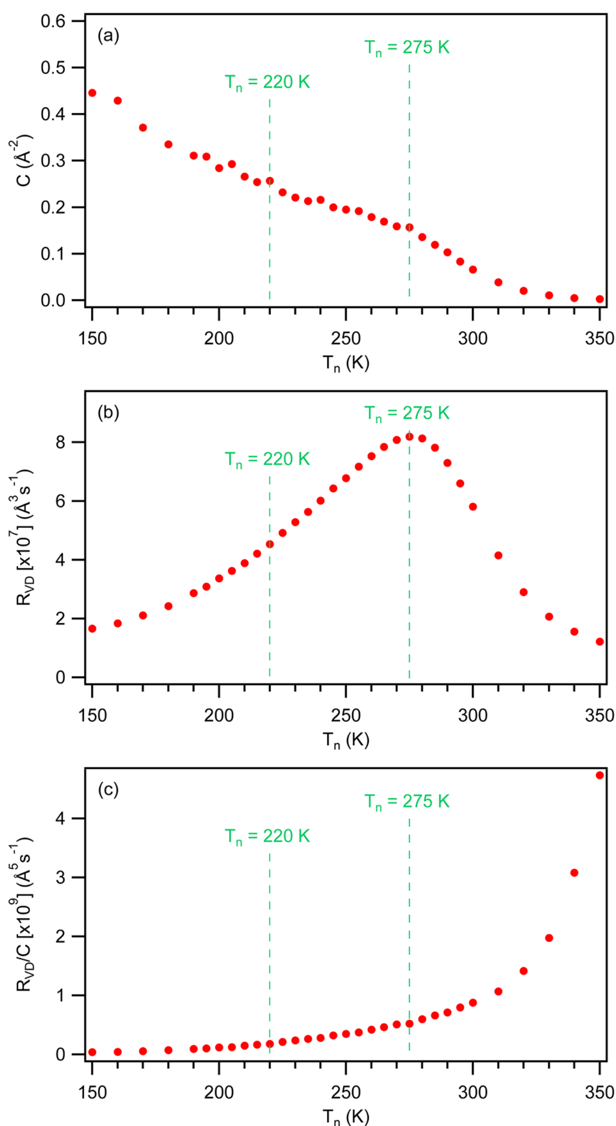

Figure 3. (a) Fluence (C) found by integrating $c(r)$ over the sink ($0 \leq r \leq r_0$) shown in Figure 2a, plotted for a number of temperatures T_n. (b and c) Corresponding plots of R_{VD} and R_{VD}/C versus T_n. The Arrhenius analysis method yields good approximations to E_D and D_0 at temperatures between ∼220 and ∼275 K.

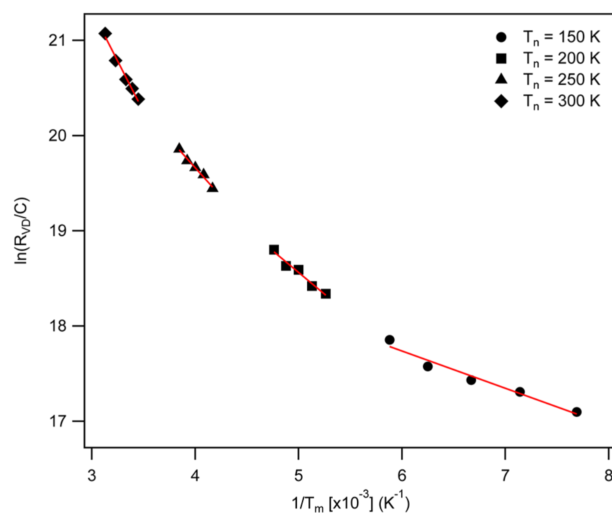

Figure 4. Arrhenius plots used to generate the data in Figure 5a at temperatures (T_n) of 150, 200, 250, and 300 K.

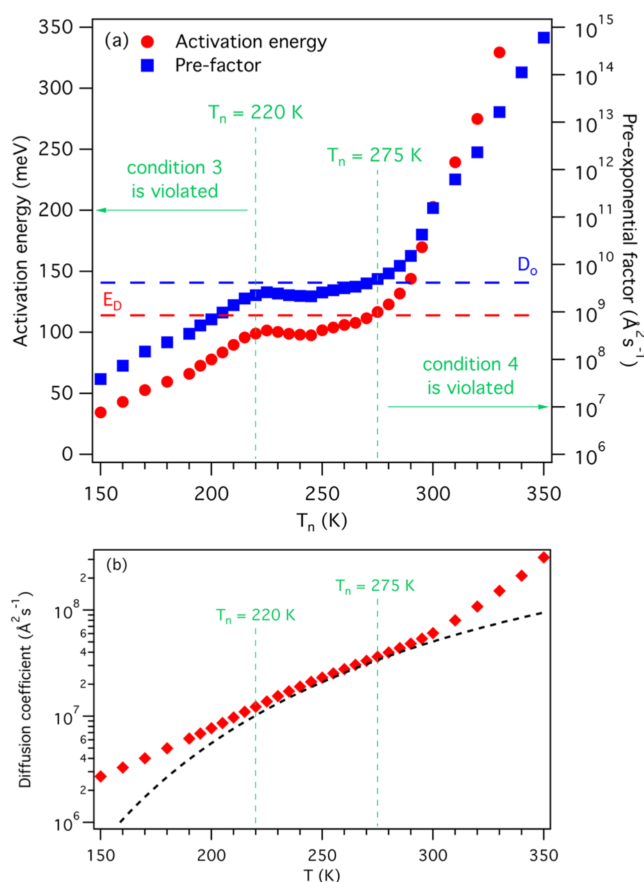

Figure 5. (a) Activation energy (red) and preexponential factor (blue) obtained by Arrhenius analysis of R_{VD}/C at a number of temperatures T_n. The quantities are approximately equal to E_D and D_0 (shown as dashed lines) over the temperature window $220 \lesssim T_n \lesssim 275$ K. (b) Diffusion coefficient (D) versus temperature (dashed black curve) and diffusion coefficients (red diamonds) calculated using the activation energies and preexponential factors in part a.

The quantities V, σ, and $f(r,T)$ must also be known because they appear in eq 10. The electron flux profile $f(r,T)$ is a function of T because it includes electrons emitted from the deposit at each temperature used to generate the Arrhenius plot (e.g., see how the deposit geometry changes with T in Figure 1). It can be obtained using Monte Carlo simulations of electron−solid interactions[27−29] and the geometries of deposits grown by EBID. If the dissociation cross section σ is not known, it can be approximated by analysis of the EBID growth rates.[17]

Extraction of Diffusion Energies and Preexponential Factors. Figure 5a shows plots of the activation energies and preexponential factors obtained by Arrhenius analyses of R_{VD} at a number of temperatures T_n. The corresponding diffusion coefficients are shown in Figure 5b. Each point n was generated as follows:

(i) EBID was simulated at each of the temperatures (T_n) plotted in Figure 5a in order to obtain a set of deposits and the corresponding vertical growth rates $R(r,T_n)$. Such data can be obtained experimentally by performing EBID as a function of the substrate temperature.

DOI: 10.1021/acsami.5b06341
ACS Appl. Mater. Interfaces 2015, 7, 21408−21415

(ii) $N_a(r,T_n)$ was calculated using eq 10 and using the values of V and σ used in the simulations. These values must be known if this procedure is applied to experimental data, as must $f(r,T_n)$. The latter can be obtained using Monte Carlo simulations of electron trajectories in the deposit made at each temperature.

(iii) $C(T_n)$, shown in Figure 3a, was calculated by substituting $N_a(r,T_n)$ into eq 7 and integrating $c(r,T_n)$ over $0 \leq r \leq r_0$.

(iv) R_{VD}, shown in Figure 3b, was calculated by performing each simulation with and without diffusion and by taking the difference between the resulting simulated volumes. It was analyzed on the basis of eq 8. An experimental method for the measurement of R_{VD} is discussed below.

(v) An Arrhenius plot of $\ln(R_{VD}/C)$ was produced for each temperature T_n, using growth rate data from five temperatures T_m centered on T_n (i.e., $m = n + i$, where i is an integer in the range of −2 and +2). Figure 4 shows these plots for T_n = 150, 200, 250, and 300 K.

(vi) The slope of each Arrhenius plot yields an activation energy [multiplied by $-1/(k_BT_n)$] and a preexponential factor (multiplied by V), as per eq 9.

The data in Figure 5a show that the activation energies and preexponential factors obtained using this procedure are good approximations to E_D and D_0 over a particular temperature range, which in this case is $220 \lesssim T_n \lesssim 275$ K (the "true" values E_D = 114 meV and $D_0 = 4.16 \times 10^9$ Å^2/s, shown as dashed lines on the plot, are those that were used in the model[13] that was used to simulate EBID in the first step of the above procedure). We note that the method appears to produce correct diffusion coefficients (Figure 5b) at temperatures between ∼275 and ∼300 K because, in this temperature range, errors in the activation energy and preexponential factor offset each other when eq 3 is used to calculate D.

The reasons for why the Arrhenius analysis method fails at temperatures that are too high or too low are discussed in detail below.

Prerequisites. Arrhenius analysis can be used to extract E_D and D_0 if the following set of conditions is satisfied at each temperature T_n used to perform EBID:

(1) *Steady-state growth condition*: The vertical growth rate must be constant: $\partial R/\partial t \approx 0$.

(2) *Significant adsorbate concentration gradient condition*: Adsorbate coverage must be low near the beam axis (as $r \to 0$) and high far away from the beam ($r \to \infty$).

(3) *Diffusion-dominated replenishment condition*: Adsorbate replenishment near the deposit periphery (i.e., near r_0, shown in Figure 2a) must be dominated by diffusion, which is satisfied when $D\nabla^2 N_a \gg sF$ in the vicinity of r_0.

(4) *Efficient adsorbate consumption condition*: In-diffusing adsorbates (i.e., those diffusing from the source to the sink shown in Figure 2a) must be dissociated by electrons, which is satisfied when $\sigma f \gg 1/\tau$.

In the following, we discuss each condition and explain why the Arrhenius analysis method fails when any one of them is not satisfied.

Condition 1: Steady-State Growth. During the early stages of EBID, $R(r)$ changes with time as the surface irradiated by the electron beam evolves from that of a horizontal plane into a structure that eventually grows at a constant rate antiparallel to the electron beam (as discussed in refs 13 and 30−32). The growth rates used for Arrhenius analysis must be measured in the steady state so that changes in R_{VD}/C with T are caused purely by the temperature dependence of D and are not affected by the temperature dependence of the transition from the initial state to the steady state. Experimentally, attainment of a steady state can be verified simply by fabricating a set of deposits as a function of the growth time and by measuring $R(r,t)$. Models such as the one used here output the time evolution of $R(r)$; hence, it is easy to ensure that condition 1 is satisfied, and the results in Figure 5a were obtained in the steady state.

Condition 2: Significant Adsorbate Concentration Gradient. Adsorbate depletion under the electron beam is needed in order to generate a concentration gradient that gives rise to net flow of surface-adsorbed precursor molecules. In the absence of a concentration gradient, $c(r) \approx 0$, and diffusion does not contribute to EBID.[2,13] In the opposite extreme, illustrated for the case of the Langmuir isotherm in Figure 2b, $\Theta(r\to 0) \approx 0$ and $\Theta(r\to\infty) \approx 1$, R_{VD} is maximized and, hence, errors associated with the measurement of R_{VD} are minimized.

Significant depletion $[\Theta(r \to 0) \approx 0]$ occurs in the so-called *mass-transport-limited growth regime*, where the adsorbate dissociation rate is much greater than the adsorbate replenishment rate:[1] $\sigma f \gg sF/N_a + \tau^{-1}$. This condition is realized by using a high electron-beam-current density.

Far away from the beam, adsorbate coverage is saturated [i.e., $\Theta(r\to\infty) \approx 1$] when the adsorption rate is much greater than the thermal desorption rate: $sF \gg N_a/\tau$. This condition is realized by using a high precursor gas pressure.

The data in Figure 5a were obtained in the limit of high depletion and are not affected by condition 2. To demonstrate what happens when the adsorbate concentration gradient is too small, Figure 6 shows a plot of C as a function of the electron beam current (for a beam diameter of 100 nm). The extent of depletion, defined as the percentage $100[1 - \Theta(r\to 0)/\Theta(r\to\infty)]$, is shown on the top axis. The data show that $C \approx 0$ in the reaction-rate-limited growth regime and that it increases with the electron beam current in the mass-transport-limited growth regime. The Arrhenius analysis method obviously fails as $C \to 0$.

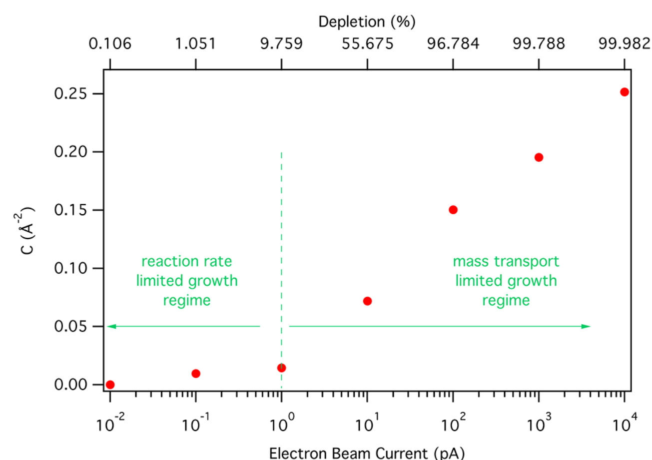

Figure 6. Fluence C plotted as a function of the electron beam current.

Condition 3: Diffusion-Dominated Replenishment. Adsorbates diffusing from the source to the sink shown in Figure 2a give rise to the formation of the rings seen in Figure 1 and to R_{VD}. However, vacant surface sites in the sink are also populated by gas molecules adsorbing from the gas phase. Hence, the growth rate of the ring is dominated by the diffusing

DOI: 10.1021/acsami.5b06341
ACS Appl. Mater. Interfaces 2015, 7, 21408−21415

adsorbates only if $D\nabla^2 N_a \gg sF$ (in the vicinity of r_0). If this condition is not satisfied (i.e., if the diffusion rate is too low because T is too low), then R_{VD} has a significant contribution from sF and the magnitude of this contribution increases with decreasing T. The net effect is seen in Figure 3b as a reduction in the slope of $R_{VD}(T)$ below ∼220 K. Consequently, the Arrhenius analysis method fails at low temperatures (see Figure 5a) because the temperature dependence of R_{VD}/C is not dominated by the temperature dependence of D (which is defined by eq 3).

To confirm that the failure of the Arrhenius analysis method at low temperatures is caused by a violation of condition 3, Figure 7 shows a plot of the maximum flux of diffusing adsorbates ($\max[D\nabla^2 N_a(r)]$) versus T_n. The plot reveals that this flux is equal to the adsorption flux (sF) at ∼200 K. That is, the condition $D\nabla^2 N_a \gg sF$ is violated as the five-point temperature window used to generate each point T_n in Figure 5a approaches 200 K.

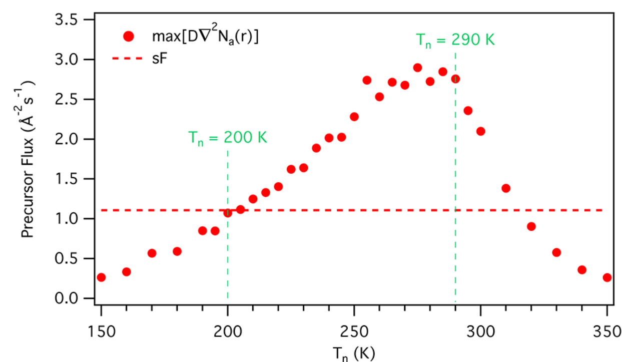

Figure 7. Maximum flux of diffusing adsorbates ($\max[D\nabla^2 N_a(r)]$) plotted at a number of temperatures T_n. The adsorption flux (sF) is shown as a dashed horizontal line.

We note that, at temperatures in excess of ∼290 K, the plot in Figure 7 shows that $\max[D\nabla^2 N_a(r)]$ rapidly decreases with increasing T. This is caused by depopulation of the surface through thermal desorption, which compromises the Arrhenius analysis method because the EBID rate approaches zero as $N_a \to 0$. This effect contributes to the failure of the method at high temperatures seen in Figure 5a. However, the failure at high temperatures is also contributed to by condition 4, which is discussed below.

A plot equivalent to Figure 7 can be generated using experimental EBID data and can therefore be used to find the range of temperatures over which condition 3 is satisfied.

Condition 4: Efficient Adsorbate Consumption. The driving force of diffusion $c(r)$ defines the net mass transport of adsorbates from the source to the sink shown in Figure 2a. However, the in-diffusing adsorbates must not desorb (term N_a/τ in eq 1) but must instead be dissociated by electrons (term $\sigma f N_a$) in order to be consumed in the EBID reaction and contribute to R_{VD}. Hence, if the condition $\sigma f \gg 1/\tau$ is not satisfied (i.e., if the residence time of adsorbates at the surface is too short because the temperature is too high), then both R_{VD} and C are reduced by an amount that scales with T due to the exponential dependence of $1/\tau$ on T (eq 2). This effect is seen in Figure 3a,b, where it causes abrupt changes in the slopes of $C(T)$ and $R_{VD}(T)$ at temperatures greater than ∼275 K. Consequently, the Arrhenius analysis method fails at high temperatures (see Figure 5a) because the temperature dependence of R_{VD}/C is not dominated by the temperature dependence of D.

We note that the plot of R_{VD} on T_n in Figure 3b reveals that R_{VD} increases with T up to 275 K, beyond which it decays with increasing T. The general shape of this curve is a consequence of two competing exponential dependencies on the temperature: the increase in D with T defined by eq 3 and the decrease in τ with T defined by eq 2. The rapid decay in $R_{VD}(T)$ at high temperatures is caused by a violation of condition 4 (i.e., desorption of in-diffusing adsorbates), which becomes significant at 275 K, and is distinct from the thermal depopulation of the surface seen in Figure 7, which is insignificant below ∼290 K.

Experimentally, the maximum temperature at which condition 4 is satisfied can be found using plots of $C(T)$ and $R_{VD}(T)$ analogous to those shown in Figure 3.

Limitations of the Arrhenius Analysis Method. We have demonstrated that E_D and D_0 can be found by Arrhenius analysis of the nanostructure growth rates provided the analysis is performed over a specific temperature window. Within this window (shown in Figure 5a), the mean errors in E_D and D_0 are 9% and 30%, respectively. The latter is greater because D_0 is obtained from the y intercepts of the Arrhenius plots shown in Figure 4, where the vertical axis is $\ln(R_{VD}/C)$. The mean error in $\ln(D_0)$ is smaller than 2%.

The valid temperature window is defined by the temperature dependence of $\ln(R_{VD}/C)$. Specifically, within the window, conditions 3 and 4 are satisfied and the temperature dependence of $\ln(R_{VD}/C)$ is dominated by that of D (given by eq 3). Outside the window, the method fails because the temperature dependence of $\ln(R_{VD}/C)$ changes as condition 3 and/or 4 is violated. The method also fails if the nanostructure growth rates are not measured in the steady state (condition 1) or the electron-beam-current density and, hence, the extent of adsorbate depletion is too low (condition 2). If all four conditions are satisfied, uncertainties in E_D and D_0 are dominated by the noise in $c(r)$ profiles (see Figure 2a) because of the ∇^2 operator in eq 7. Hence, in practice, nanostructure geometries (i.e., growth rates) must be measured to a high degree of accuracy in order to minimize the noise in $c(r)$.

The width of the valid temperature window is system-specific (e.g., it is affected by the corrugation factor[23] E_D/E_a) and can be maximized by tuning the precursor pressure and electron-beam-current density.

Finally, we note that deployment of the proposed method requires an experimental procedure for the attainment of $R_{VD}(T_n)$. The simplest procedure is to collect a set of $R(r,T_n)$ profiles such as that shown in Figure 1b, subtract the lowest temperature profile $R(r,T_{min})$ from each $R(r,T_n)$, and integrate the resulting curves over r to get $R_{VD}(T_n)$. To demonstrate the validity of this approach, we used our simulated $R(r,T_n)$ profiles to obtain $R_{VD}(T_n)$ using T_{min} values of 120 and 150 K. Figure 8 shows the resulting plots of the activation energy and preexponential factor versus T_n. It shows that the analysis method works but T_{min} affects the width of the valid temperature window (as expected), which is characterized by a plateau in each curve. We note that the dependencies of the activation energy and prefactor on T_n beyond the plateau depend on the method used to obtain R_{VD}, as is seen by the differences between the results in Figures 8 and 5a. This is a consequence of the effects of T_{min} and a violation of condition 4 on the diffusion-free component of the growth rate (produced by adsorption from the gas phase) at low and high T_n,

DOI: 10.1021/acsami.5b06341
ACS Appl. Mater. Interfaces 2015, 7, 21408−21415

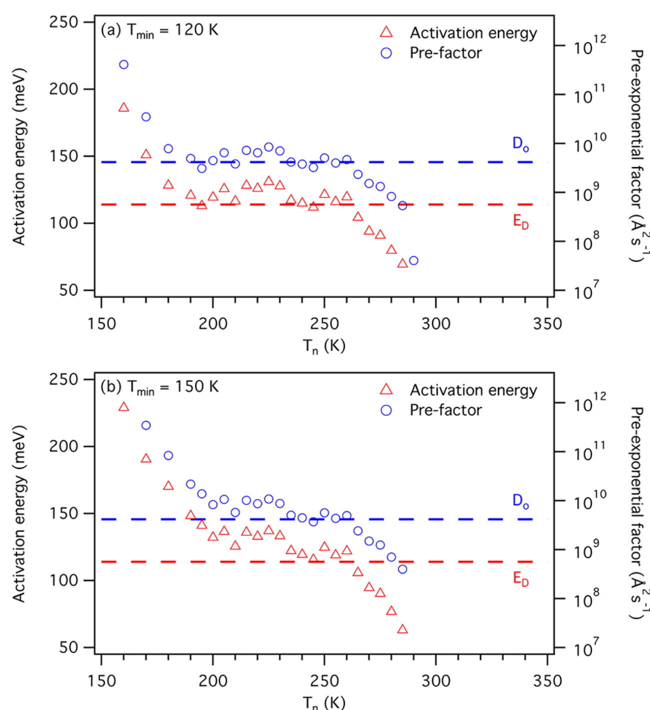

Figure 8. Activation energy (red) and preexponential factor (blue) obtained by Arrhenius analysis of R_{VD}/C at a number of temperatures T_n. The volume $R_{VD}(T_n)$ was estimated by subtracting (a) $R(r,T_{min}=120\ K)$ and (a) $R(r,T_{min}=150\ K)$ from each $R(r,T_n)$ profile and integrating the resulting curves over r.

respectively. The minimum temperature that can be used to perform conventional EBID (rather than cryogenic EBID[33,34]) is limited by adsorbate condensation onto the substrate. Condensation (i.e., the formation of multilayers rather than Langmuir adsorption defined by the term $1 - \Theta$ in eq 1) was ignored in our analysis (however, the precursor condensation temperature is easy to find and avoid experimentally[14,33,34]). More generally, the analysis presented here must be redone for systems that do not exhibit Langmuir adsorption and systems in which coverage-dependent phenomena such as adsorbate–adsorbate interactions are significant (i.e., such effects must be incorporated into eq 1).

CONCLUSION

Using a hybrid continuum–Monte Carlo model of EBID, we have developed a method that enables the calculation of diffusion energies and preexponential factors by Arrhenius analysis of the nanostructure deposition rates. The method is valid under specific growth conditions that were defined quantitatively. Our results pave the way for experimental studies of adsorbate diffusion by EBID.

AUTHOR INFORMATION

Corresponding Author

*E-mail: Milos.Toth@uts.edu.au.

Notes

The authors declare no competing financial interest.

ACKNOWLEDGMENTS

This work was funded by FEI Company and the Australian Research Council (Project DP140102721). This research was undertaken with the assistance of resources provided at the NCI National Facility systems at the Australian National University through the National Computational Merit Allocation Scheme supported by the Australian Government.

REFERENCES

(1) Toth, M.; Lobo, C. J.; Friedli, V.; Szkudlarek, A.; Utke, I. Continuum Models of Focused Electron Beam Induced Processing. *Beilstein J. Nanotechnol.* **2015**, *6*, 1518–1540.
(2) Utke, I.; Moshkalev, S.; Russell, P. *Nanofabrication Using Focused Ion and Electron Beams; Principles and Applications*; Oxford University Press: New York, 2012.
(3) Huth, M.; Porrati, F.; Schwalb, C.; Winhold, M.; Sachser, R.; Dukic, M.; Adams, J.; Fantner, G. Focused Electron Beam Induced Deposition: A Perspective. *Beilstein J. Nanotechnol.* **2012**, *3*, 597–619.
(4) Randolph, S. J.; Fowlkes, J. D.; Rack, P. D. Focused, Nanoscale Electron-Beam-Induced Deposition and Etching. *Crit. Rev. Solid State Mater. Sci.* **2006**, *31*, 55–89.
(5) van Dorp, W. F.; Hagen, C. W. A Critical Literature Review of Focused Electron Beam Induced Deposition. *J. Appl. Phys.* **2008**, *104*, 081301.
(6) Lee, E.-K.; Song, J.-H.; Jeong, K.-Y.; Kang, J.-H.; Park, H.-G.; Seo, M.-K. Resonant Light Scattering from a Single Dielectric Nano-Antenna Formed By Electron Beam-Induced Deposition. *Sci. Rep.* **2015**, *5*, 10400.
(7) Acar, H.; Coenen, T.; Polman, A.; Kuipers, L. K. Dispersive Ground Plane Core-Shell Type Optical Monopole Antennas Fabricated with Electron Beam Induced Deposition. *ACS Nano* **2012**, *6*, 8226–8232.
(8) Ivanov, A. P.; Freedman, K. J.; Kim, M. J.; Albrecht, T.; Edel, J. B. High Precision Fabrication and Positioning of Nanoelectrodes in a Nanopore. *ACS Nano* **2014**, *8*, 1940–1948.
(9) Fernández-Pacheco, A.; Serrano-Ramón, L.; Michalik, J. M.; Ibarra, M. R.; De Teresa, J. M.; O'Brien, L.; Petit, D.; Lee, J.; Cowburn, R. P. Three Dimensional Magnetic Nanowires Grown by Focused Electron-Beam Induced Deposition. *Sci. Rep.* **2013**, *3*, 1–5.
(10) Tang, H.; Wang, X.; Xiong, Y.; Zhao, Y.; Zhang, Y.; Zhang, Y.; Yang, J.; Xu, D. Thermoelectric Characterization of Individual Bismuth Selenide Topological Insulator Nanoribbons. *Nanoscale* **2015**, *7*, 6683–6690.
(11) Gopal, V.; Radmilovic, V. R.; Daraio, C.; Jin, S.; Yang, P. D.; Stach, E. A. Rapid Prototyping of Site-Specific Nanocontacts by Electron and Ion Beam Assisted Direct-Write Nanolithography. *Nano Lett.* **2004**, *4*, 2059–2063.
(12) Toth, M. Advances in Gas-Mediated Electron Beam-Induced Etching and Related Material Processing Techniques. *Appl. Phys. A: Mater. Sci. Process.* **2014**, *117*, 1623–1629.
(13) Cullen, J.; Bahm, A.; Lobo, C. J.; Ford, M. J.; Toth, M. Localized Probing of Gas Molecule Adsorption Energies and Desorption Attempt Frequencies. *J. Phys. Chem. C* **2015**, *119*, 15948–15953.
(14) Martin, A. A.; Toth, M. Cryogenic Electron Beam Induced Chemical Etching. *ACS Appl. Mater. Interfaces* **2014**, *6*, 18457–18460.
(15) Bishop, J.; Lobo, C. J.; Martin, A.; Ford, M.; Phillips, M. R.; Toth, M. The Role of Activated Chemisorption in Electron Beam Induced Deposition. *Phys. Rev. Lett.* **2012**, *109*, 146103.
(16) Szkudlarek, A.; Gabureac, M.; Utke, I. Determination of the Surface Diffusion Coefficient and the Residence Time of Adsorbates via Local Focused Electron Beam Induced Chemical Vapour Deposition. *J. Nanosci. Nanotechnol.* **2011**, *11*, 8074–8078.
(17) Fowlkes, J. D.; Rack, P. D. Fundamental Electron-Precursor-Solid Interactions Derived from Time-Dependent Electron-Beam-Induced Deposition Simulations and Experiments. *ACS Nano* **2010**, *4*, 1619–1629.
(18) van Dorp, W. F.; Wnuk, J. D.; Gorham, J. M.; Fairbrother, D. H.; Madey, T. E.; Hagen, C. W. Electron Induced Dissociation of Trimethyl (Methylcyclopentadienyl) Platinum (IV): Total Cross Section as a Function of Incident Electron Energy. *J. Appl. Phys.* **2009**, *106*, 074903.

(19) Utke, I.; Friedli, V.; Purrucker, M.; Michler, J. Resolution in Focused Electron- and Ion-Beam Induced Processing. *J. Vac. Sci. Technol. B* **2007**, *25*, 2219−2223.
(20) Randolph, S. J.; Fowlkes, J. D.; Rack, P. D. Effects of Heat Generation During Electron-Beam-Induced Deposition of Nanostructures. *J. Appl. Phys.* **2005**, *97*, 124312.
(21) Scheuer, V.; Koops, H.; Tschudi, T. Electron Beam Decomposition of Carbonyls on Silicon. *Microelectron. Eng.* **1986**, *5*, 423−430.
(22) Christy, R. W. Formation of Thin Polymer Films by Electron Bombardment. *J. Appl. Phys.* **1960**, *31*, 1680−1683.
(23) Seebauer, E. G.; Allen, C. E. Estimating Surface Diffusion Coefficients. *Prog. Surf. Sci.* **1995**, *49*, 265−330.
(24) Barth, J. V. Transport of Adsorbates at Metal Surfaces: From Thermal Migration to Hot Precursors. *Surf. Sci. Rep.* **2000**, *40*, 75−149.
(25) Shen, J.; Muthukumar, K.; Jeschke, H. O.; Valenti, R. Physisorption of an Organometallic Platinum Complex on Silica: An Ab Initiostudy. *New J. Phys.* **2012**, *14*, 073040.
(26) Winkler, R.; Fowlkes, J.; Szkudlarek, A.; Utke, I.; Rack, P. D.; Plank, H. The Nanoscale Implications of a Molecular Gas Beam during Electron Beam Induced Deposition. *ACS Appl. Mater. Interfaces* **2014**, *6*, 2987−2995.
(27) Joy, D. C. *Monte Carlo Modeling for Electron Microscopy and Microanalysis*; Oxford University Press: New York, 1995.
(28) Hovington, P.; Drouin, D.; Gauvin, R.; Joy, D. C.; Evens, N. CASINO: A New Monte Carlo Code in C Language for Electron Beam Interaction−Part I: Description of the Program. *Scanning* **1997**, *19*, 1−14.
(29) Kuhr, J. C.; Fitting, H. J. Monte Carlo Simulation of Electron Emission from Solids. *J. Electron Spectrosc. Relat. Phenom.* **1999**, *105*, 257−273.
(30) Smith, D. A.; Fowlkes, J. D.; Rack, P. D. A Nanoscale Three-Dimensional Monte Carlo Simulation of Electron-Beam-Induced Deposition with Gas Dynamics. *Nanotechnology* **2007**, *18*, 265308.
(31) Smith, D. A.; Fowlkes, J. D.; Rack, P. D. Understanding the Kinetics and Nanoscale Morphology of Electron-Beam-Induced Deposition via a Three-Dimensional Monte Carlo Simulation: The Effects of the Precursor Molecule and the Deposited Material. *Small* **2008**, *4*, 1382−1389.
(32) Choi, Y. R. Y. R.; Rack, P. D. P. D.; Randolph, S. J. S. J.; Smith, D. a. D. A.; Joy, D. C. D. C. Pressure Effect of Growing with Electron Beam-Induced Deposition with Tungsten Hexafluoride and Tetraethylorthosilicate Precursor. *Scanning* **2006**, *28*, 311−318.
(33) Bresin, M.; Toth, M.; Dunn, K. A. Direct-Write 3D Nanolithography at Cryogenic Temperatures. *Nanotechnology* **2013**, *24*, 035301.
(34) Bresin, M.; Thiel, B. L.; Toth, M.; Dunn, K. A. Focused Electron Beam-Induced Deposition at Cryogenic Temperatures. *J. Mater. Res.* **2011**, *26*, 357−364.

DOI: 10.1021/acsami.5b06341
ACS Appl. Mater. Interfaces 2015, 7, 21408−21415